Mitigating low-temperature hydrothermal degradation of 2 mol% yttria stabilised zirconia and of 3 mol% yttria stabilised zirconia/nickel oxide by calcium oxide co-doping and two-step sintering

Taubmann, Julian; Frandsen, Henrik Lund; Khajavi, Peyman

Published in:
Ceramics International

Link to article, DOI:
10.1016/j.ceramint.2024.08.162

Publication date:
2024

Document Version
Publisher's PDF, also known as Version of record

Ceramics International 50 (2024) 43108–43121

Contents lists available at ScienceDirect

Ceramics International

journal homepage: www.elsevier.com/locate/ceramint

Mitigating low-temperature hydrothermal degradation of 2 mol% yttria stabilised zirconia and of 3 mol% yttria stabilised zirconia/nickel oxide by calcium oxide co-doping and two-step sintering

Julian Taubmann *, Henrik Lund Frandsen, Peyman Khajavi

Department of Energy Conversion and Storage, Technical University of Denmark, Fysikvej, Lyngby, DK-2800, Denmark

ARTICLE INFO

Keywords:
Hydrothermal degradation
Tetragonal zirconia
Calcium oxide co-doping
Two-step sintering
Solid oxide cells

ABSTRACT

Hydrothermal degradation deteriorates the fracture toughness and strength of tetragonal stabilised zirconia. The phase transformation to the monoclinic phase is particularly critical for materials with lower stabiliser content such as 2 mol% and 3 mol% yttria stabilised zirconia (2YSZ and 3YSZ). In this work, two routes in two-step sintering and co-doping with calcium oxide are analysed to mitigate the degradation. Both strategies show a reduction in average grain size of the 2YSZ while maintaining a comparable densification. The achieved smaller grains suppress the hydrothermal degradation rates. In addition, a mitigating effect beyond the reduction in grain size of YSZ is found for CaO doping. 1.6 mol% CaO co-doped 2YSZ shows less than 4% of monoclinic phase after 50 h in an autoclave with H_2O at 134 °C. Pure 2YSZ contrarily reaches 100% monoclinic phase after 20 h at the same conditions. A suppression of degradation by CaO doping was also observed for the composite of nickel oxide and 3 mol% yttria stabilised zirconia. Hence, CaO co-doping can be an interesting strategy to increase resistivity against hydrothermal degradation for both biomedical and renewable energy applications. The findings further outline a route to achieve tetragonal YSZ with lower yttria contents than 2 mol%.

1. Introduction

Stabilised zirconia ceramics comprise a wide spectrum of applications, ranging from biomedical implants [1–4] over thermal barrier coatings [5,6] to electrolytes and mechanical support structures in solid oxide cells (SOC) [7–9].

Each application has specific properties sought after in zirconia, for example ionic conductivity of the cubic phase [9] or mechanical strength of the tetragonal phase [2,4]. In general, pure zirconia at atmospheric pressure exhibits three allotropic crystal structures in monoclinic (m), tetragonal (t), and cubic (c) [10]. The three phases display temperature dependent stability in pure zirconia, starting with monoclinic up to 1170 °C, transforming into tetragonal, that is finally stable up to 2370 °C, whereas cubic prevails at temperatures above to the melting point [3]. A stabilisation of the cubic or tetragonal phase down to room temperature (RT) can be achieved by doping zirconia with a variety of oxides, as for example in yttria (Y_2O_3) stabilised zirconia (YSZ) [11]. In addition, in zirconia stabilised by an aliovalent dopant (e.g. Y^{3+} or Sc^{3+}), oxygen vacancies form due to charge compensation from the aliovalent cations compared to the tetravalent Zr [12–15].

When zirconia is applied for its mechanical properties, the metastable tetragonal phase is sought after, which can be stabilised by doping smaller amounts of stabilisers compared to the cubic phase, for example equal or less than 3 mol% of Y_2O_3 [3,10]. This metastability of tetragonal YSZ means that the phase can transform into the monoclinic phase under mechanical stress [16]. At a crack tip of a tetragonal YSZ ceramic, the transformation of t- into m-phase acts to resist crack propagation. This termed transformation toughening stems from the volume expansion induced by the phase transformation and introduces compressive stresses [17].

Despite the outstanding fracture toughness and strength of t-YSZ due to transformation toughening, the transformation into the m-phase can also have detrimental effects [10]. This generally termed low-temperature hydrothermal degradation (LTD) of t-YSZ was first reported by Kobayashi et al. for t-YSZ in humid atmospheres at 250 °C [18]. LTD starts with a slow transformation of tetragonal into monoclinic phase at the surface [10,18]. This is followed by microcracking, surface-roughening, and grain pullout at the surface and ultimately, leads to a loss of strength of the material [18–20].

* Corresponding author.
E-mail address: julta@dtu.dk (J. Taubmann).

https://doi.org/10.1016/j.ceramint.2024.08.162
Received 8 February 2024; Received in revised form 30 July 2024; Accepted 9 August 2024
Available online 14 August 2024

The proposed degradation mechanisms all consider the important role of oxygen vacancies in the lattice of the tetragonal stabilised zirconia [21–23]. The vacancies are characteristic for the crystal phase and its stability, while further being preferred sites for H_2O adsorption and dissociation [21–24]. An uptake of, e.g. hydroxyls from the surface, can then alter the defect/oxygen vacancy concentration necessary to destabilise the t-phase and to cause the transformation into the m-phase with a lower defect concentration [23,25]. Changes in the surface structure (crack formation, roughening) can subsequently lead to LTD progressing into the bulk of zirconia [10].

In order to mitigate LTD, the grain size of t-YSZ is one of the main handles investigated. It has proven that tetragonal YSZ with a smaller average grain size is more resistive against LTD [3,20,26,27]. A smaller grain size of t-YSZ can be achieved by co-doping with other oxides [19]. Some examples of applied co-dopants are Al_2O_3 [28,29], SiO_2 [28], La_2O_3 [26], and CeO_2 [30]. As a general trend, co-doped cations with larger ionic radius result in smaller grains due to enhanced surface and grain boundary segregation while sintering the stabilised zirconia (SZ) [31,32]. However, some co-doping, e.g. by La_2O_3, can reduce densification of YSZ, harming its functional properties [33].

In addition, the sintering temperature can be used to control grain growth [19,34]. Several studies indicate an increased degradation of polycrystalline tetragonal SZ after sintering at higher temperatures caused by enlarged grains. This can ultimately degrade the mechanical strength and toughness [3,19,34,35]. Therefore, a reduction in sintering temperature can improve resistivity against LTD.

However, a mere decrease in sintering temperature can be an unfeasible route for reducing grain sizes because of limited densification at lower temperatures [36]. Lower densification of SZ significantly reduces the toughness and strength, which are often desired functional properties of tetragonal SZ [2,20,37]. Moreover, porosity due to lower densification results in H_2O penetrating the bulk and reacting on the increased surface area. Porosity is also undesirable for biomedical applications, e.g. in dental implants [2].

A balance must hence be found between small average grains by reduced sintering temperatures while maintaining sufficient densification. Here, multi-step sintering profiles have shown promise for controlling densification [19] and grain growth in stabilised zirconia [38]. These implications have further been linked to lower rates of LTD and improved strength and toughness of SZ [39,40].

In the present work, both co-doping of t-YSZ and two-step sintering are applied to study and suppress LTD of 2 mol% yttria stabilised zirconia (2YSZ). 2YSZ demonstrates outstanding fracture toughness and strength due to a high transformability [41–43]. For example, the fracture toughness of 2YSZ (8.6 MPa $m^{1/2}$) compared with 3YSZ (4.1 MPa $m^{1/2}$) is more than twice as high [43]. 2YSZ is however prone to rapid LTD in humid atmospheres due to the low concentration of stabiliser in the zirconia lattice [3,27,43]. To that effect, 2YSZ is less widely researched and research often focuses on tetragonal YSZ with higher yttria contents (e.g. 3YSZ).

Nonetheless, an ageing-resistant 2YSZ can be paramount for applications in which transformation toughening plays a key role, and tetragonal YSZ with lowest yttria content is sought after. Therefore, the study assesses the role of co-doping with calcium oxide and two-step sintering for a possible mitigation of the low temperature hydrothermal degradation. CaO stabilisation of ZrO_2 has previously shown to result in small grain sizes (around 100 nm when sintered at 1300 °C) and lower degradation rates compared with tetragonal YSZ. The approach further produced promising mechanical properties (toughness) when care is taken to omit the formation of cubic phase by sintering temperature and doping content [44,45].

To investigate the effect of the co-dopant content on 2YSZ, we used 0.4, 0.8, and 1.6 mol% CaO added to 2YSZ, allowing a quantitative comparison with the degradation of pure 2YSZ. Moreover, the effect of heat treatment on the grain growth of the plain and co-doped 2YSZ was analysed by varying sintering temperatures and applying two-step sintering profiles. To consider possible negative effects on the functional properties of 2YSZ by co-doping and two-step sintering, the densification was measured to assure comparability between specimens in terms of available surface area during degradation testing.

We further extended the study of CaO co-doping to the composite of 3YSZ and nickel oxide (NiO). This cermet is typically applied as mechanical support structure of solid oxide fuel and electrolysis cells. Even though the cells are operated at temperatures (600–900 °C) above the typically reported temperature range for LTD of RT-400 °C [10], LTD of t-YSZ in SOCs was observed previously [46,47]. Since gas atmospheres with H_2O are common as a reactant during electrolysis or as a product in fuel cell mode, the conditions resemble those of LTD reported during exposure to gaseous H_2O [10,18]. Especially during heating or cooling in humid atmospheres, rapid LTD of the composite can occur [47]. Hence, the phase transformation of the mechanical support into m-YSZ, similarly to other applications, can reduce strength of the structure up to cell failure [46,47].

2. Material and methods

2.1. Sample preparation

Commercially available powders of TZ-2Y (Tosoh, Japan) and CaO (Sigma-Aldrich, United States of America) were used in the study. The respective mixture of 0.4, 0.8, and 1.6 mol% CaO in 2YSZ was prepared by dissolving the CaO in distilled water, then adding 2YSZ and subsequently drying the powder mixture. For NiO/YSZ, nickel oxide (Inframat Advanced Materials, United States of America), TZ-3Y (Tosoh, Japan), and CaO (Sigma-Aldrich, United States of America) powder were mixed in ethanol for 24 h. The samples consisted of a NiO to 3YSZ ratio of 55 wt% to 45 wt%, as in a standard support [48] for an SOC, and were co-doped with 0.8 mol% and 1.6 mol% of CaO. The amount of CaO was added according to both NiO and 3YSZ due to the unknown interaction of CaO and NiO. Hence, the mole fraction in relation to 3YSZ was ultimately 2.3 mol% CaO for 0.8 mol% co-doped NiO/3YSZ and 4.6 mol% CaO for 1.6 mol% co-doped NiO/3YSZ.

The resulting powders were pressed to pellets in an uniaxially press (PW 10, P-O-Weber, Germany). A 50 wt% PVP (Polyvinylpyrrolidone, Sigma-Aldrich, United States of America) in water mixture was added as a binding agent for the shaping process. A uniaxial pressure of 50 MPa was applied for 30 s while forming the pellets with a thickness of 2 mm and diameter of 16.5 mm. Afterwards, the pellets were cold-isostatically pressed (Stenhøj 100, Denmark), applying a pressure of 500 MPa for 30 s.

2.2. Heat treatment

The prepared pellets were heat treated in air with three different sintering profiles. During all the programs, the samples were heated to 500 °C with a heating rate of 120 °C/h for a slow burning off of the organic additive. Afterwards, a heating rate of 360 °C/h was applied to reach the sintering temperature. Once the profiles were completed, the samples were cooled down with a rate of 360 °C/h to room temperature. The following three heat treatment programs were used in the study:

- **Program 1 (P1):** Three sintering temperatures of 1250, 1300 and 1400 °C were researched for program 1. The pellets remained for 5 h at the respective temperatures before cooling down. The programs are abbreviated in the remainder of the manuscript as P1-1250 °C, P1-1300 °C, and P1-1400 °C.
- **Program 2:** The sintering temperatures of 1400 and 1450 °C were investigated in program 2. The pellets were sintered for 0.05 h (3 min), cooling down immediately after. The programs are abbreviated as P2-1400 °C and P2-1450 °C.

- **Program 3:** A two-step sintering program was chosen as the third program, heating to the peak temperature as the first step and cooling down immediately after to the dwell-temperature as the second step. The peak temperatures were 1350 and 1400 °C with the dwell-temperature either 100 °C or 150 °C below. The first-step temperature was held for 0.05 h (3 min). Then, the furnace cooled down to the second-step temperature at which the samples annealed for 5 h. The programs are abbreviated as P3-1350-1250 °C, P3-1400-1250 °C, and P3-1400-1300 °C.

2.3. Accelerated ageing

The low temperature degradation of the samples was tested in an autoclave filled with distilled water and brought to a pressure of 2 bar at 134 °C. At the same temperature and in steam, 80% of monoclinic phase were generated over ca. 15 h for plain 3YSZ [35]. In order to assess the effect of the addition of CaO and the two-step sintering, the samples were aged over 50 h to compare the degradation rates. The exposures were interrupted after several intervals and the samples were characterised by XRD to quantify the volume fraction of the monoclinic phase.

2.4. Densification

The density of the sintered pellets was measured via the Archimedes principle. The samples were immersed in distilled water, whereas the density of the pellet can be calculated from Eq. (1).

$$\rho_p = \frac{m_p}{m_p - m_w}\,\rho_w \tag{1}$$

The density of the pellet ρ_p is given as function of the pellet weight m_p, the weight of the pellet immersed in distilled water, and the density of distilled water ρ_w. The density of each pellet was compared with the theoretical density of 6.1 g/cm^3 given for 2YSZ by the supplier (Tosoh, Japan). The mixture density in the case of co-doped 2YSZ was calculated according to the mole fractions between CaO/2YSZ and is used to determine the densification. It is further noteworthy that the Archimedes method as applied here is not ASTM (American Society for Testing and Materials) standardised since the standards for ceramics require placing the samples in boiling water, which could irreversibly degrade the samples of this study before any ageing test. Therefore, a commercially available setup (Mettler Toledo) for the assessment of densification with the Archimedes method was used. To verify this non-standardised method, the shrinkage and weight of specimens were measured to compare the densification between both methods. The results of this comparison can be seen in Fig. 3. The electron microscopy images taken from all samples surfaces further show the high densification of the specimens. The agreement of these three independent techniques indicates that the Archimedes method, as applied in this study, is accurate and can give a valid indication of the densification of the samples.

2.5. Scanning electron microscopy

The grain size of the samples was analysed using a field emission scanning electron microscope (FE-SEM, Merlin, Carl Zeiss, Germany). In order to investigate the size of the grains of each sample, the sintered pellets were polished down to sub-μm finish starting with SiC polishing discs down to dedicated fibres and a diamond polishing paste (Struer's equipment). The prepared samples were subsequently thermally etched to reveal the grains at the polished surface of the ceramics by heating them to 50 °C below the sintering temperature [49]. The grain size for each sample was subsequently determined from the diameter of approximately 350 grains from three SEM images per sample by the image processing software ImageJ. Energy dispersive X-ray spectroscopy (EDS) with a Bruker XFlash 6-60 detector was used to map the surface of the samples and to analyse possible secondary phase formation by co-doping with CaO. The acceleration voltage was 10 kV for the EDS maps and the peaks from ionisation in the O K shell at 0.525 keV, the Zr LA at 2.044 keV, the Ca KA at 3.691 keV, the Y L at 1.943 keV, and the Ni L at 0.840 keV were used.

2.6. X-ray diffraction

The crystalline phases were studied by X-ray diffraction (XRD), using a Rigaku Miniflex 600 XRD (Rigaku, Japan) with Cu-Kα radiation. The diffraction patterns were collected in the 2-theta range of 10–90° with a scan speed of 5 °/min and a step size of 0.02°. The peaks of interest are at 28.174° and 31.467° for monoclinic zirconia of the $(\bar{1}11)$ and (111) orientation and at 30.211° for tetragonal zirconia of the (101) orientation. The integrated peak areas can then be used to calculate the fraction of monoclinic to tetragonal crystal-phase after the works of Garvie and Nicholson [50] as well as Toraya et al. [51].

$$X_m = \frac{I_m(111) + I_m(\bar{1}11)}{I_m(111) + I_m(\bar{1}11) + I_t(101)} \tag{2}$$

The ratio X_m of monoclinic phase is derived according to Eq. (2) with the XRD peak intensities I and subscripts for monoclinic (m) and tetragonal phase (t), respectively.

$$V_m = \frac{1.311 X_m}{1 + 0.311 X_m} \tag{3}$$

Ultimately, Eq. (3) gives the volume fraction of monoclinic phase.

2.7. Raman spectroscopy

A Renishaw InVia Raman spectrometer system was used to acquire the Raman spectra presented in this study. The spectra were collected with a 532 nm wavelength diode laser with a laser power of less than 8 mW at the sample surface. Micro Raman spectroscopy with a 50x microscope objective (laser spot size of approximately 1 μm) was used to collect spectra at nine different locations for each sample.

2.8. Thermogravimetric analysis

Thermogravimetric analsyis (TGA) was performed to determine the amounts of $Ca(OH)_2$ and $CaCO_3$ in the CaO powder and thereby, the CaO doping content after sintering. A NETZSCH STA 449F3 was used for the thermogravimetry with an Ar atmosphere and a heating rate of 5 K/min from 20 to 800 °C.

3. Results

In the following the effect of sintering profile and addition of CaO are presented in terms of densification, grain size, and extent of hydrothermal degradation.

3.1. XRD of raw powders

The XRD of the as received powders, before preparing the respective co-doped 2YSZ and co-doped composite NiO/3YSZ mixtures, can be seen in Fig. 1. The 2YSZ and 3YSZ powders (Tosoh, Japan) show both peaks of the monoclinic and tetragonal phase. The clearly separable peaks for monoclinic in blue and tetragonal in black are indexed in Fig. 1 (a) and (b) for 2YSZ and 3YSZ. All peaks are indicated as lines beneath the XRD pattern according to files ICSD (Inorganic Crystal Structure Database) #75309 for tetragonal and ICSD#38870 for monoclinic YSZ. The XRD of the NiO powder (Inframat Advanced Materials, United States of America) in Fig. 1 (d) shows the expected cubic NiO peaks in agreement with ICSD#9866.

In Fig. 1 (c), the XRD pattern of the CaO powder (Sigma-Aldrich, United States of America) reveals additional phases ascribed to hexagonal $Ca(OH)_2$ (space group $P\bar{3}m1$; ICSD#15471) and traces of trigonal

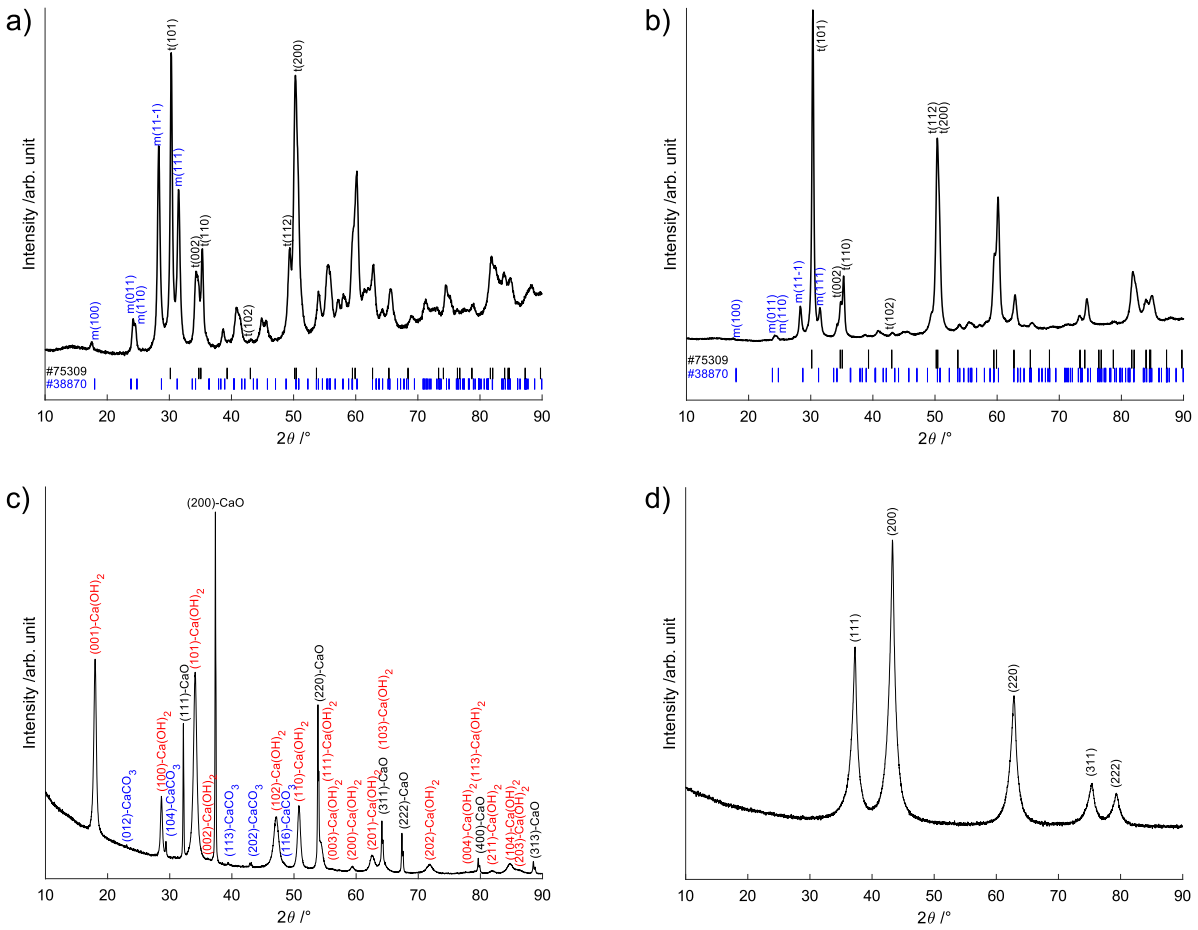

Fig. 1. XRD of the powders used in this study from (a) 2YSZ, (b) 3YSZ, (c) CaO to (d) NiO.

$CaCO_3$ (space group $R\bar{3}cH$; ICSD#20179), besides the expected cubic CaO (ICSD#14922). Both phases are not critical for the sintering process at the temperatures evaluated here, since $Ca(OH)_2$ decomposes to CaO in the range of 320–512 °C [52,53] and $CaCO_3$ to CaO in the range of 490–800 °C [53–56]. However, the composition of the powder is of importance in terms of the exact mol% of CaO doping of the final sintered pellets. Therefore, TGA was performed to assess the amount of CaO present above 800 °C, which ultimately leads to the mol% CaO co-doping reported in 0.4 mol%, 0.8 mol% and 1.6 mol%.

The TGA of the CaO powder can be seen in Fig. 2, showing the mass loss with increasing temperature. A first drop in mass is measured with the starting decomposition of $Ca(OH)_2$ around 350 °C (marked by (1)) [52,53]. The second mass loss appears around 570 °C and can be ascribed to the decomposition of $CaCO_3$ (marked by (2)) [53–55]. The larger mass loss with the $Ca(OH)_2$ decomposition agrees well with the XRD of the raw powder, that indicates mostly CaO and $Ca(OH)_2$ in the powder with only a minor fraction of $CaCO_3$.

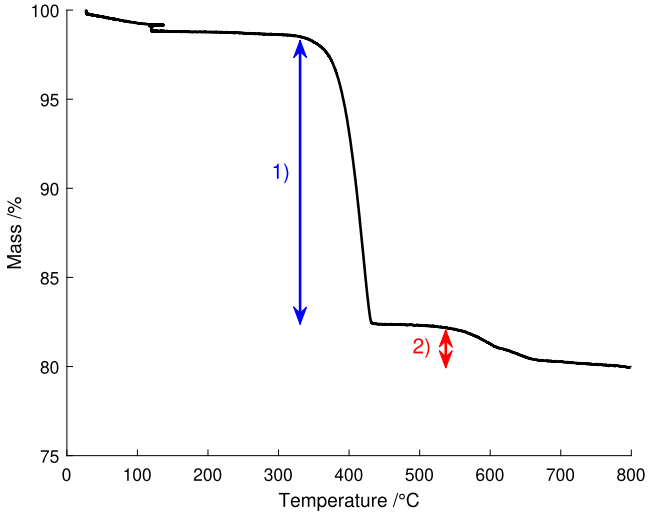

Fig. 2. TGA of the CaO powder is shown for the treatment in Ar with 5 K/min from 20 to 800 °C. The two mass losses for $Ca(OH)_2$ and $CaCO_3$ are marked by (1) and (2), respectively.

3.2. Densification

Fig. 3 displays the trends in densification according to CaO content and sintering profile. To confirm the applicability of the Archimedes method for the samples of this study, the densification was measured based on the geometry and weight of the samples, which is shown in Fig. 3 as black bars for P1-1300 °C and P1-1400 °C. Further, the high densification can be visually confirmed by the SEM images taken from all the sample surfaces.

Following observations can be made:

(1) The densification increases with higher sintering temperatures, starting at values around 95% for P1-1250 °C and increasing to values around 99% densification for P1-1400 °C.

(2) The different sintering profiles (P1, P2, and P3) produce differing densification. For example, the comparison between P1-1400 °C and P2-1400 °C shows a 1% higher densification for P1 and an annealing time of 5 h over 3 min for P2. However, a similar densification around 99% is reached with the two-step sintering profile of P3-1400-1300 °C. This is despite of the annealing time in P3 at 1400 °C

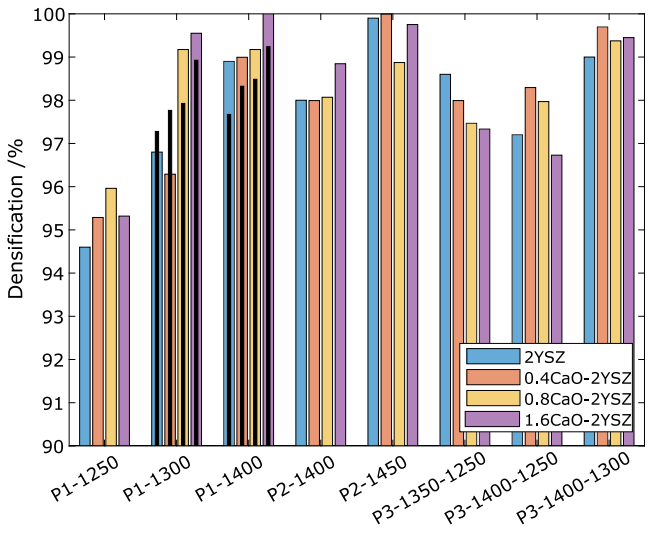

Fig. 3. The densification listed for each sintering program and CaO content. For P1-1300 and P1-1400 °C, the densification determined from the shrinkage and weight is given as a reference by the black bars.

matching the time in P2. The 5 h dwell time at 1300 °C proofs beneficial in terms of densification. A higher temperature for P2, as in P2-1450 °C, increases densification to values comparable with P1-1400 °C. This indicates that a higher peak sintering temperature can compensate for shorter dwell times during sintering. The two-step sintering profiles P3-1350-1250 °C and P3-1400-1250 °C showcase the importance of the second step in two-step sintering. A 2% lower densification is achieved with the second temperature being 1250 °C instead of 1300 °C.

(3) At peak sintering temperatures above 1300 °C, the co-doping with CaO shows no effect on the densification with increasing CaO content. A sintering temperature of 1250 °C results in the lowest densification for 1.6 mol% CaO. The discrepancies with the next lowest densification are in the range of 0.2 to 2%.

An important observation is the insignificance of the addition of CaO on the densification of the samples. An enhanced porosity of samples could ultimately affect the degradation by an increased surface area for a reaction and/or diffusion of water or reaction intermediates leading to the onset of hydrothermal degradation [2,57]. A lower densification could additionally decrease the mechanical properties of SZ [2,5]. Thus, these results allow the comparison of degradation rates of different sintering profiles and CaO contents.

3.3. Grain size

The grain size of stabilised zirconia is an important descriptor for the stability against hydrothermal degradation. To determine the grain size distribution, the grains of each sample were quantified via SEM images. Even without analysing the grain sizes in the respective SEM images, a clear distinction is visible between the surface of pure 2YSZ and 1.6 mol% CaO co-doped 2YSZ. This can be seen in Fig. 4 in which four SEM images visualise the grains of (a) plain 2YSZ and (b) 1.6 mol% CaO doped 2YSZ sintered by P3-1350-1250 °C and for the profile P1-1250 °C in (c) pure 2YSZ and (d) 1.6 mol% CaO co-doped 2YSZ.

Less variations in grain size throughout the SEM image are visible for the 1.6 mol% CaO co-doped sample. In Fig. 5, the grain size distributions of P1-1250 °C and P3-1350 °C–1250 °C are illustrated for plain 2YSZ and 1.6 mol% CaO co-doped 2YSZ. All grain size distributions were also fitted to a respective log-normal distribution. The distribution of both heat treatment profiles becomes narrower and moves towards smaller grain sizes for samples with 1.6 mol% CaO compared to pure 2YSZ.

Table 1 summarises the average grain sizes of the six different sintering profiles and for plain 2YSZ, 0.4 mol%, 0.8 mol%, and 1.6 mol% CaO co-doped 2YSZ. The sintering profiles of P1-1250 °C, P1-1400 °C, P2-1400°, P2-1450 °C, P3-1350-1250 °C, and P3-1400-1250 °C are listed, and the standard deviation is given in brackets behind the average grain size. A decreasing average grain size can be seen in Table 1 with increasing mole fraction of CaO. The trend is independent of sintering profile and sintering temperature. Highest average grain sizes are always found for pure 2YSZ and the size decreases with enhancing the mole fraction of CaO.

The sample P2-1400 °C depicts an outlier of the trend with a stagnant average grain size between 0.8 mol% and 1.6 mol% of CaO. Since this was not observed for any other sintering profile, it seems to be influenced by the limitations in the measurement of grain sizes restricted to micrometre sized surface areas rather than a limit of smallest grain size for P2-1400 °C.

The choice of sintering temperature and profile influences the grain size and in general, a higher sintering temperature leads to larger grains. The annealing time at the sintering temperature further affects the size of the grains. This can be seen in the comparison between P1-1400 °C and P2-1400 °C in which 3 min at 1400 °C in P2 create smaller grains than with a dwell time of 5 h in P1.

Furthermore, the highest temperature, even for 3 min, defines the average grain distribution more than any dwell time at a lower temperature afterwards. This can be seen for P2-1400 °C and P3-1400-1250 °C. There, the temperature of 1400 °C produces similar grain sizes across all CaO contents and the 5 h dwell time during P3 has only a minor effect, as it can be seen for 0.4 and 0.8 mol% CaO with 9–13 nm smaller grains with P2.

These two cases indicate the dominant role of the first step of the two-step sintering on the grain growth of 2YSZ. The importance of the first sintering step agrees well with what was previously found, for example for cubic-YSZ sintered by two-step profiles [39]. The size of the grains is therefore largely defined by the highest temperature a sample experiences instead of the time the sample remains at a lower sintering temperature afterwards.

The extent of grain size reduction between sintering profiles for 1.6 mol% CaO doped 2YSZ and pure 2YSZ can be determined as 38% for P1-1250 °C, 29% for P1-1400 °C, 35% for P2-1400 °C, and 35% for P3-1400 °C-1250 °C. The lowest value of 29% for the 5 h sintering time at 1400 °C indicates a decrease in average grains size reduction at higher sintering temperatures.

3.4. Hydrothermal degradation

The initial crystalline structure of all 2YSZ-CaO samples was assessed by XRD before the start of the hydrothermal ageing tests and compared to references for monoclinic and tetragonal zirconia provided by the ICSD (Inorganic Crystal Structure Database) and ICDD (International Centre for Diffraction Data) with file numbers 37-1484 for monoclinic and 00-060-0502 for tetragonal zirconia, respectively. The observed peaks are indexed accordingly in Fig. 6 (a) for the sintering program P1-1300 °C. It becomes apparent, that besides the tetragonal peaks of 2YSZ, the pure 2YSZ shows initial monoclinic phase correlating to ca. 5% monoclinic fraction across all pure 2YSZ samples.

Raman spectroscopy was applied as a confirmatory technique for the crystal phases assigned by XRD. This is exemplified in Fig. 6 (b) for samples sintered by P1-1300 °C, revealing all typically observed peaks at 147, 261, 318, 463, 611, and 641 cm^{-1} for tetragonal zirconia (marked in Fig. 6 (b) by black lines with t-ZrO_2), as for example assigned in Refs. [58,59]. The strong Raman bands for monoclinic zirconia at 179, 191 and 478 cm^{-1} are marked as well as two weaker bands (381 and 537 cm^{-1}) that are not overlapping with tetragonal peaks and are hence visible (marked by blue lines with m-ZrO_2 in Fig. 6 (b)) [60]. The monoclinic peaks only appear, to a locally varying extent as observed by micro-Raman spectroscopy, in the pure 2YSZ

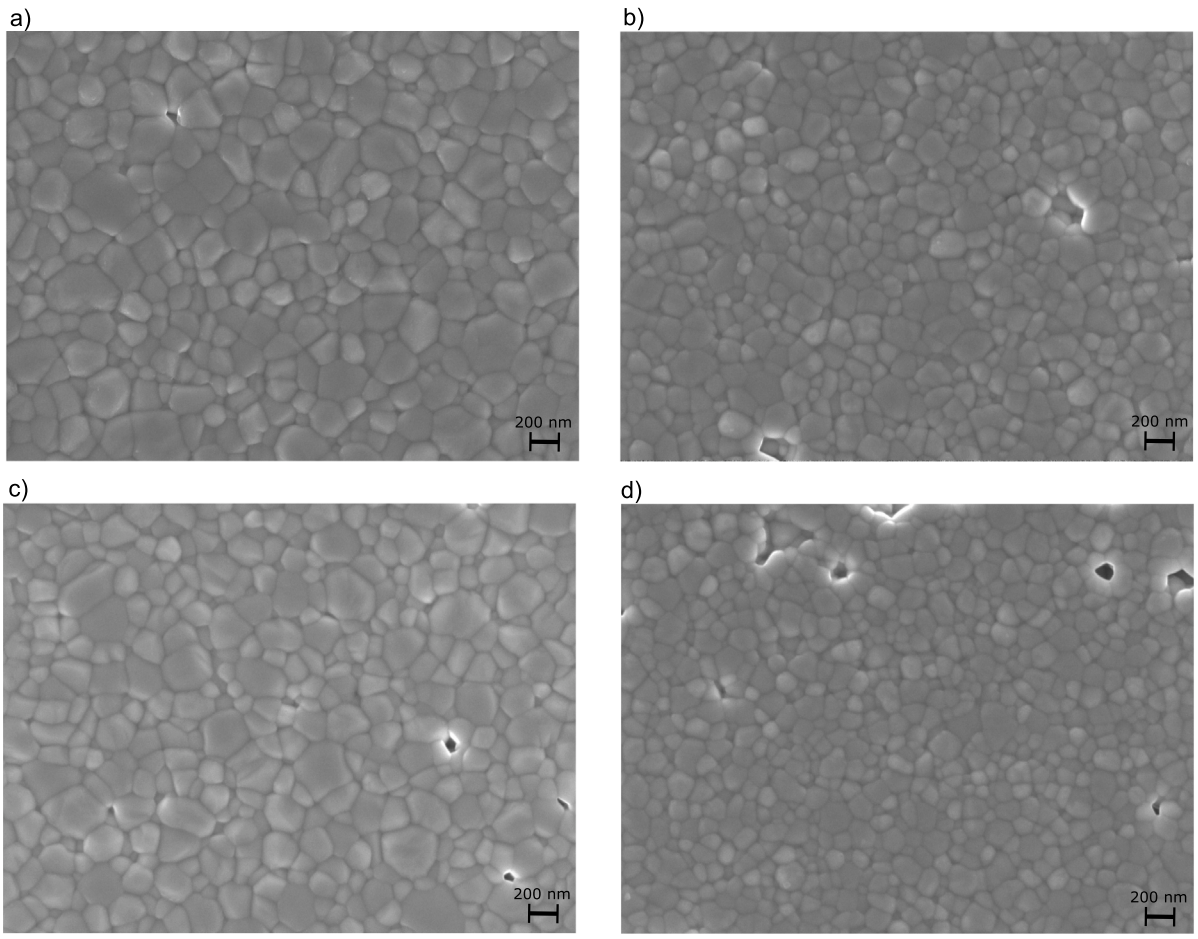

Fig. 4. SEM images to illustrate the grain sizes of (a) pure 2YSZ and (b) 1.6 mol% CaO co-doped 2YSZ sintered with P1-1250 °C as well as (c) 2YSZ and (d) 1.6 mol% CaO co-doped 2YSZ sintered with P3-1350-1250 °C.

Table 1
Averaged grain size of sintering programs P1-1250 °C, P1-1400 °C, P2-1400 °C, P2-1450 °C, P3-1350-1250 °C, and P3-1400 °C-1250 °C listed for pure 2YSZ, 0.4 mol% CaO, 0.8 mol% CaO, and 1.6 mol% CaO co-doped 2YSZ. The standard deviation of the grain size is given in brackets behind the grain size.

	2YSZ	0.4CaO-2YSZ	0.8CaO-2YSZ	1.6CaO-2YSZ
P1-1250 °C	199 nm (±73 nm)	173 nm (±63 nm)	138 nm (±58 nm)	123 nm (±42 nm)
P1-1400 °C	288 nm (±113 nm)	232 nm (±96 nm)	242 nm (±101 nm)	205 nm (±83 nm)
P2-1400 °C	252 nm (±79 nm)	199 nm (±69 nm)	164 nm (±61 nm)	164 nm (±53 nm)
P2-1450 °C	279 nm (±100 nm)	252 nm (±74 nm)	237 nm (±73 nm)	201 nm (±63 nm)
P3-1350-1250 °C	203 nm (±79 nm)	165 nm (±61 nm)	147 nm (±57 nm)	132 nm (±46 nm)
P3-1400-1250 °C	249 nm (±83 nm)	208 nm (±56 nm)	177 nm (±65 nm)	163 nm (±44 nm)

samples. This agrees with the findings from XRD, which only showed a monoclinic fraction in the pure 2YSZ case, and related literature on CaO doping of ZrO_2 in Ref. [60].

The XRD results in the characteristic range of 27–32° 2θ depict the increasing monoclinic volume fraction over the ageing time during LTD. In Fig. 7, the evolution of the three peaks is shown for the sintering profile of P2-1450 °C and for pure 2YSZ (solid line) as well as 1.6 mol% CaO doped 2YSZ (dotted line) over the course of 19 h with XRD measurements after 3 h and 9 h. The $(\bar{1}11)$ monoclinic and (101) tetragonal SZ peaks are shifted to the left from the expected positions at 28.174° and 30.211° in Fig. 7 due to the sample height not being perfectly aligned for the XRD measurements. The shift is uniform for the peaks and only the integrated peak areas are used for the monoclinic phase calculations. Therefore, the analysis of the monoclinic fraction remains valid. In addition, the correct peak position can indeed be measured as illustrated by the XRD collected on the pristine samples in Fig. 6, confirming the correct assignment of monoclinic and tetragonal SZ phases.

Fig. 8 (a), (b) and (c) summarises the evolution of the monoclinic fraction for plain 2YSZ, 0.4 mol%, 0.8 mol%, and 1.6 mol% CaO co-doped 2YSZ sintered with (a) P1-1250 °C, (b) P3-1350-1250 °C and (c) P2-1450 °C. Both figures illustrate the reduced transformation of tetragonal zirconia into the monoclinic phase with the addition of CaO. The samples with 0.4 mol% added CaO show a slightly suppressed degradation rate, reaching a complete monoclinic phase content after around 10 h. Samples containing 0.8 mol% CaO delay the phase transformation further while propagating to a volume fraction of ca. 90% after 50 h. In the case of 1.6 mol% CaO co-doped 2YSZ, the XRD measurements reveal less than 4% monoclinic phase for all sintering profiles after the test duration of 50 h.

Fig. 8 shows that the transformation of samples with 0.4 mol% CaO is only slightly suppressed as can be seen in (a) and (b) with comparable degradation rates to pure 2YSZ or an absent effect as in (c). The rapid and immediate onset of phase-transformation in pure 2YSZ was previously reported [26]. In this study, the initially present monoclinic

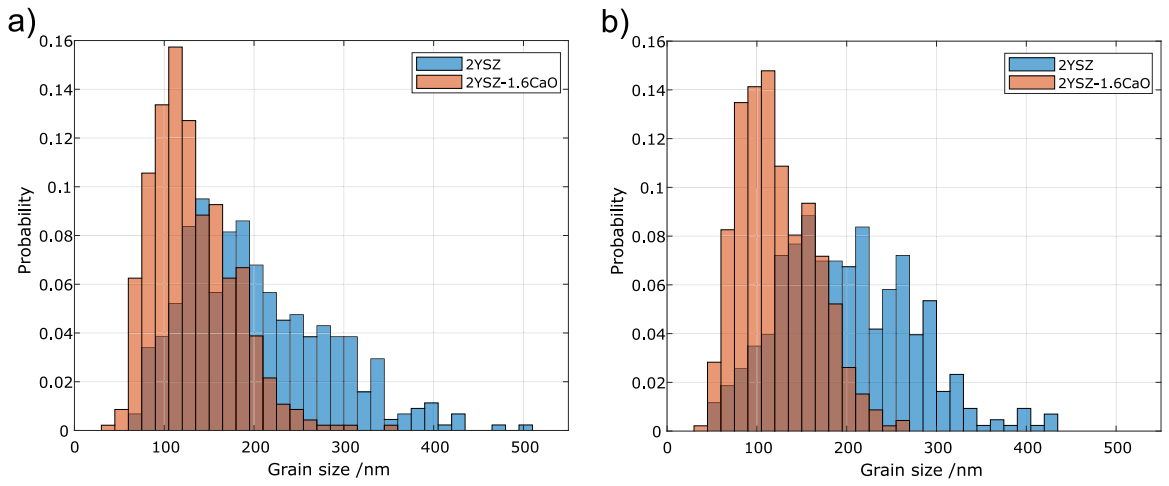

Fig. 5. Grain size distributions of sintering program P1-1250 °C in (a) and program P3-1350-1250 °C in (b) depicted for pure 2YSZ and 1.6 mol% CaO co-doped 2YSZ.

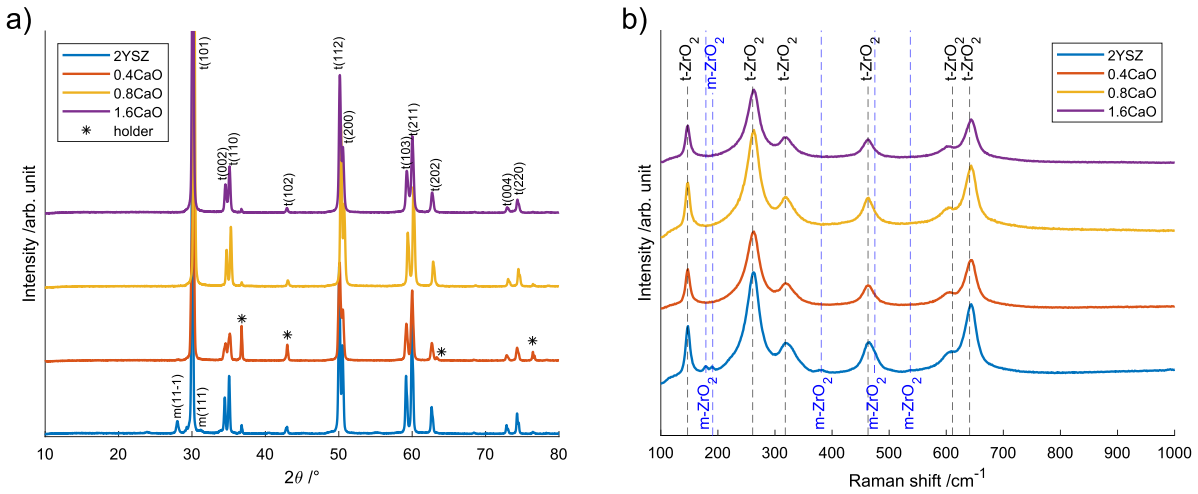

Fig. 6. XRD of samples of different CaO co-dopant contents sintered with program P1-1300 °C in (a) and respective Raman spectra for the same samples in (b). XRD peaks for tetragonal (t), monoclinic (m) and the sample holder (holder) are indexed as well as characteristic Raman spectroscopy peaks for tetragonal SZ (t-ZrO_2) and monoclinic SZ (m-ZrO_2).

volume fraction for pure 2YSZ in the range of 5% is further noteworthy. The sintering profile has no observable effect on the initial monoclinic fraction. This can be ascribed to the smaller grain size of 2YSZ sintered at lower temperatures (P1-1250 °C) as well as the stabilising effect of high densification for high temperature sintered samples (P2-1450 °C). The latter was previously ascribed to the decreasing elastic modulus with higher porosity (free surface energy), which can destabilise the tetragonal phase during cooling down after sintering [61,62].

Parts (a), (b) and (c) of Fig. 8 illustrate similar degradation profiles. The slightly smaller grain sizes of P1-1250 °C seem not to result in any observable suppression of LTD. On the contrary, the samples of P3-1350-1250 °C show a slower rate of LTD in the cases of pure 2YSZ and 0.4 mol% CaO. P2-1450 °C possesses an even slower LTD rate for pure 2YSZ than P3 and P1 and a similar rate for 0.4 and 0.8 mol% CaO. 1.6 mol% CaO co-doped 2YSZ demonstrates a comparable rate between all three sintering profiles and the monoclinic fraction is less than 4% after 50 h.

3.5. Ageing kinetics

The ageing kinetics of tetragonal zirconia in terms of formation of monoclinic phase, expressed by the monoclinic volume fraction V_m, can be described by the Mehl–Avarami–Johnson formalism [10,12]. The analysis yields characteristic ageing parameters in n related to the geometry of the transformation and b as the kinetic rate of tetragonal to monoclinic transformation [27,63]. The parameters can be acquired by fitting the following function to the ageing profiles of 2YSZ and CaO doped 2YSZ prepared with different sintering profiles.

$$\frac{V_m - V_{m,0}}{V_{m,sat} - V_{m,0}} = 1 - exp\left(-(b\,t)^n\right) \tag{4}$$

In the equation above, the initial volume fraction $V_{m,0}$, the saturation volume fraction $V_{m,sat}$ of monoclinic phase are used to determine the rate of phase transformation from tetragonal to monoclinic.

The extracted parameter and initial and final volume fraction of monoclinic phase can be found in Table 2 for P1-1250 °C, P3-1350-1250 °C, and P2-1450 °C. All the samples reached a monoclinic saturation volume fraction close to 100% after the 50 h test period with the exception of 1.6 mol% CaO co-doped 2YSZ which remained below 4%. One outlier is the pure 2YSZ sample sintered with P1-1250 °C, which became too brittle and crumbled before completing the full transformation to monoclinic.

For most of the specimens, the n value decreases with CaO content. This trend is similar to related research on the addition of La_2O_3 to 3YSZ [27]. The values from Zhang et al. [27] are given as reference in Table 2. The degradation rate b also decreases with increasing the CaO content, following the trends of the degradation curves. For the 0.8 mol% CaO co-doped samples, the highest b value is observed for the

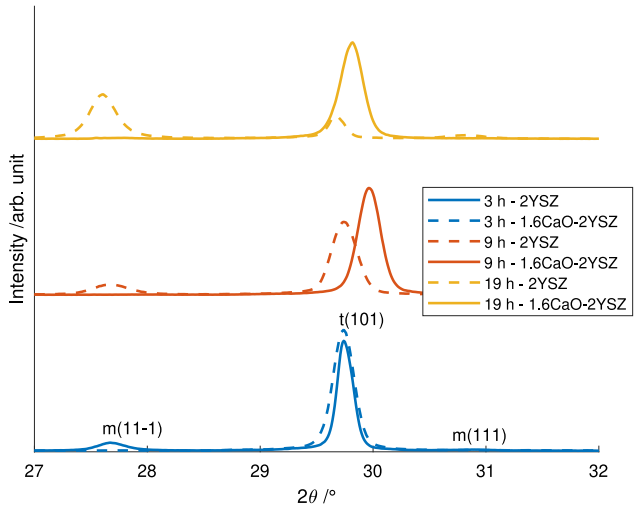

Fig. 7. XRD of the sintering program P2-1450 °C for 2YSZ (solid line) and 1.6 mol% CaO co-doped 2YSZ (dashed line) highlight the evolution of the pattern up to 19 h. The peaks for monoclinic SZ (m-SZ) and tetragonal SZ (t-SZ) are indexed accordingly.

Table 2
Parameters of the ageing kinetics listed for P1-1250 °C, P3-1350 °C-1250 °C, and P2-1450 °C and 2YSZ, 0.4 mol% CaO, 0.8 mol% CaO, and 1.6 mol% CaO co-doped 2YSZ, respectively. The parameters are the geometry factor n, the kinetic rate b, the initial monoclinic volume fraction $V_{m,0}$, and the saturation monoclinic volume fraction $V_{m,sat}$. In brackets behind the values, the parameters for pure 3YSZ (next to pure 2YSZ), 1 mol% La_2O_3 co-doped 3YSZ (next to 0.8 mol% CaO), and 2 mol% La_2O_3 co-doped 3YSZ (next to 1.6 mol% CaO) can be found as a reference according to Zhang et al. [27].

P1-1250 °C				
	2YSZ	2YSZ-0.4CaO	2YSZ-0.8CaO	2YSZ-1.6CaO
n	–	1.93	1.89 (1.3)	1.63 (1.3)
b [h^{-1}]	–	0.109	0.046 (0.09)	0.069 (0.057)
$V_{m,0}$ [%]	3.2	0.8	0.0	0.0
$V_{m,sat}$ [%]	73.2	96.7	93.4	0.7
P3-1350 °C-1250 °C				
	2YSZ	2YSZ-0.4CaO	2YSZ-0.8CaO	2YSZ-1.6CaO
n	1.39 (1.53)	1.76	2.39 (1.3)	0.98 (1.3)
b [h^{-1}]	0.125 (0.114)	0.116	0.055 (0.09)	0.063 (0.057)
$V_{m,0}$ [%]	6.0	0.0	0.0	0.0
$V_{m,sat}$ [%]	98.7	98.4	94.3	2.8
P2-1450 °C				
	2YSZ	2YSZ-0.4CaO	2YSZ-0.8CaO	2YSZ-1.6CaO
n	2.47 (1.53)	2.30	2.04 (1.3)	2.98 (1.3)
b [h^{-1}]	0.060 (0.114)	0.080	0.055 (0.09)	0.039 (0.057)
$V_{m,0}$ [%]	4.0	0.6	0.0	0.0
$V_{m,sat}$ [%]	96.2	97.1	96.1	3.7

lowest sintering temperature of 1250 °C with smallest average grains. The rates are even more reduced than for the 1mol% La_2O_3 co-doped 3YSZ [27] (brackets in Table 2), which as a plain material is more resistant to LTD than 2YSZ. The lower sintering temperatures of the 2YSZ investigated in this study also lead to lower rates of degradation b (here below 0.3 h^{-1}) in comparison with a previous study on 2YSZ, which reported $b = 0.5$ h^{-1} for 2YSZ sintered 2 h at 1450 °C [43].

3.6. Composite NiO/3YSZ

In terms of mitigating LTD in the composite of NiO/3YSZ, the effect of CaO on the grain growth shows a similar trend as for 2YSZ. The average grain size of 3YSZ in NiO/3YSZ is found to be 234 nm, whereas the 0.8 mol% CaO co-doped sample has an average of 185 nm sintered with P1-1300 °C. Both values are larger compared to 203 nm of pure 2YSZ and 147 nm of 0.8 mol% CaO co-doped 2YSZ sintered with P3-1350-1250 °C. The grain size distribution of NiO/3YSZ becomes narrower and the average grain size reduces due to the presence of 0.8 mol% CaO. The densification remains high for the 0.8 mol% co-doped samples with 95% compared to 96% for the plain NiO/3YSZ.

The initial crystalline structure of all samples was investigated by XRD, as is shown in Fig. 9 (a) for pure NiO/3YSZ and the CaO co-doped samples. The characteristic orientations of tetragonal and cubic zirconia as well as cubic NiO are marked in Fig. 9 (a) according to ICSD and ICDD files (00-060-0502 for tetragonal and 30-1468 for cubic zirconia). As a confirmatory technique of the crystal structure, Raman spectroscopy was applied as shown in Fig. 9 (b) with the characteristic peaks for tetragonal SZ (as mentioned above in the 2YSZ section) and NiO marked following established literature [58,59,64]. The characteristic NiO first order modes at 420 and 520 cm^{-1}, and second order modes at 700, 906, and 1090 cm^{-1} are marked by the blue lines in Fig. 9 (b) [64,65].

Both techniques indicate fully tetragonal 3YSZ in the pure NiO/3YSZ case. The XRD analysis further reveals some cubic stabilised zirconia, which can be attributed to the high CaO content, especially for the 1.6 mol% CaO co-doped sample. The additional peaks at 34.8, 59.7 and 73.7° are highlighted in Fig. 9 (c) for cubic stabilised zirconia. However, the results of Raman spectroscopy with characteristic peaks for tetragonal zirconia indicate that the majority of grains still remains tetragonal.

Comparing XRD results of ageing after 124 h in Fig. 9 (d), a more pronounced monoclinic peak, at 28–28.5°, is visible indicating the effect of the smaller grain size of the 0.8 mol% CaO co-doped sample. The respective monoclinic fractions are 3.9% for pure NiO/3YSZ and 1.1% for 0.8 mol% CaO co-doped NiO/3YSZ after 124 h. The results are consistent with the findings for 2YSZ that CaO doping suppresses LTD.

While 0.8 mol% co-doping causes no secondary phase formation, when co-doping with 1.6 mol% CaO, a secondary phase can be found by SEM at the surface covering the grains of 3YSZ, as it can be seen in Fig. 10. An analysis of the grain size was hence not possible and it seems a complete solubility of 1.6 mol% CaO in 3YSZ cannot be reached. The secondary phase can be analysed by comparing back scattering SEM images of pure NiO/3YSZ in (1a) and 1.6 mol% CaO co-doped NiO/3YSZ in (2a) of Fig. 9. The back-scattering SEM images show in (2a) a secondary phase of different contrast than the NiO and 3YSZ phases visible in (1a). Energy dispersive X-ray spectroscopy mapping of the surface reveals that the secondary phase consists of Ca and O, as can be seen when comparing image (1b) and (2b) in Fig. 10.

4. Discussion

4.1. Densification of 2YSZ

Densification is of importance in assuring comparability of LTD results between different sintering profiles and CaO contents. Indeed, some co-doping is known to suppress densification, as it is the case for La_2O_3 in 3YSZ [33]. Furthermore, secondary phase formation was found for Al_2O_3 co-doped 3YSZ. In that instance, the solubility limit of Al_2O_3 in 3YSZ is surpassed and a secondary phase forms [43]. In this study, no secondary phase formation is found for CaO doping of 2YSZ and the densification is not affected compared with pure 2YSZ.

None of the investigated sintering profiles generate 2YSZ that has a densification below 95% and mostly closed porosity can be expected [36]. Even the sample exposed to the lowest sintering temperature with P1-1250 °C reaches a densification of 95%, independent of the CaO content.

The two-step sintering programs increase densification slightly by 1%–2% over sintering profiles without the first step at an increased temperature. Nonetheless to analyse clear effects of two-step sintering, the temperatures should be lowered to a range were a clear

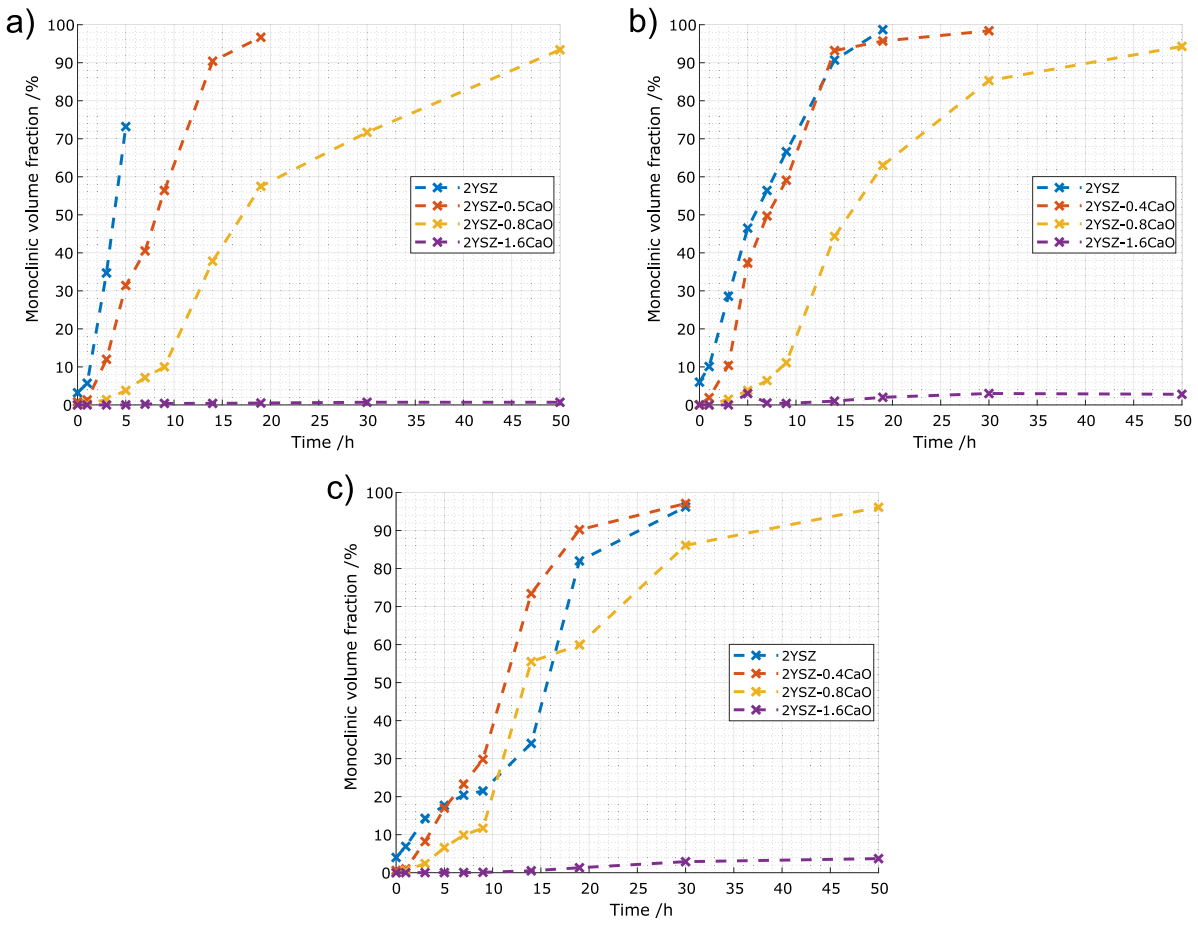

Fig. 8. LTD profiles shown for samples of the sintering program P1-1250 °C in (a), P3-1350-1250 °C in (b), and P2-1450 °C in (c). The monoclinic volume fraction was measured initially, after 1 h, 3 h, 5 h, 7 h, 9 h, 14 h, 19 h, 30 h, and 50 h. Dashed lines are merely to guide the eye and are not representative of the evolution of the volume fraction in between measurements.

effect of two-step sintering on the densification can be observed (< 1200 °C). This was not pursued here since 1250 °C is already 150-200 °C lower than the typically applied sintering temperature for 2YSZ and 3YSZ [43]. It can be regarded as an interesting side note that densification above 95% can be reached at such sintering temperatures and should be considered in future studies.

Still, the comparison of two-step sintering to conventional sintering shows that annealing times at, for example 1400 °C, can be reduced from 5 h to 3 min with subsequent annealing at 1300 °C to reach similar densification. Moreover, short annealing times (around 3 min) can result in comparable densification for 2YSZ without the need for energy intensive sintering for several hours.

The higher degradation rates b of sample sintered at lower temperatures emphasise the role of pores and densification in LTD of 2YSZ. Since pure 2YSZ sintered with P1-1250 °C displays an average grain size of 199 nm compared with 279 nm for P2-1450 °C, a higher resistance against LTD could be expected. The analysis of degradation profiles and rates depicts however the contrary and a lower rate for P2-1450 °C can be observed. The densification of 99.9% of the 1450 °C sample can be understood to confine LTD to the surface, whereas the densification of 94.6% for P1-1250° allows LTD to progress over a larger surface area which causes more rapid degradation.

These findings agree with previous studies, which showed higher stability of the tetragonal YSZ with lower porosity due to the higher elastic modulus (reduced free surface energy) [61,62]. This showcases the synergistic relationship between densification and grain size in mitigating LTD of 2YSZ in a macroscopic frame, where not only small grains define the LTD rate.

4.2. Grain growth/size of 2YSZ

The co-doping with calcium oxide reduces the average grain size up to 35% for 1.6 mol% CaO co-doped 2YSZ. Ca [66,67] and other dopants (e.g. Y in YSZ [68] and La in YSZ [27]) of SZ are known to segregate to grain boundaries and to affect grain growth [36]. The variation of CaO contents from 0.4 to 0.8 and up to 1.6 mol% confirms this for 2YSZ and the suppression of grain growth follows the CaO content.

The trend in grain size is nonetheless contradictory to results of other co-dopants in tetragonal YSZ. For Nd_2O_3 co-doping, the grain size reduced in the range of 0.1–0.4 mol% and increased with higher contents due to formation of cubic and tetragonal t' grains, Sc_2O_3 co-doping increased grain size, and secondary phase formation and reduced density was found with La_2O_3 doping [27,33]. None of this is observed for CaO doping and the phases are not detected in the CaO-2YSZ system. As can be seen in Fig. 11 with absent XRD peaks for t'(004) and c(004) in the 2θ range of 72–76°.

The stability of the tetragonal phase explains the trend of decreasing grain size with CaO content and smallest grains for 1.6 mol% CaO co-doped 2YSZ. In addition, the co-doping leaves no initial monoclinic phase, contrarily to pure 2YSZ that shows around 5% of monoclinic phase, independent of the sintering temperature applied.

4.3. LTD of 2YSZ

The trends in grain size distribution correlate with the rate and extent of hydrothermal degradation and ageing kinetics of 2YSZ. A smaller average grain size leads to a lower extent and suppressed rate

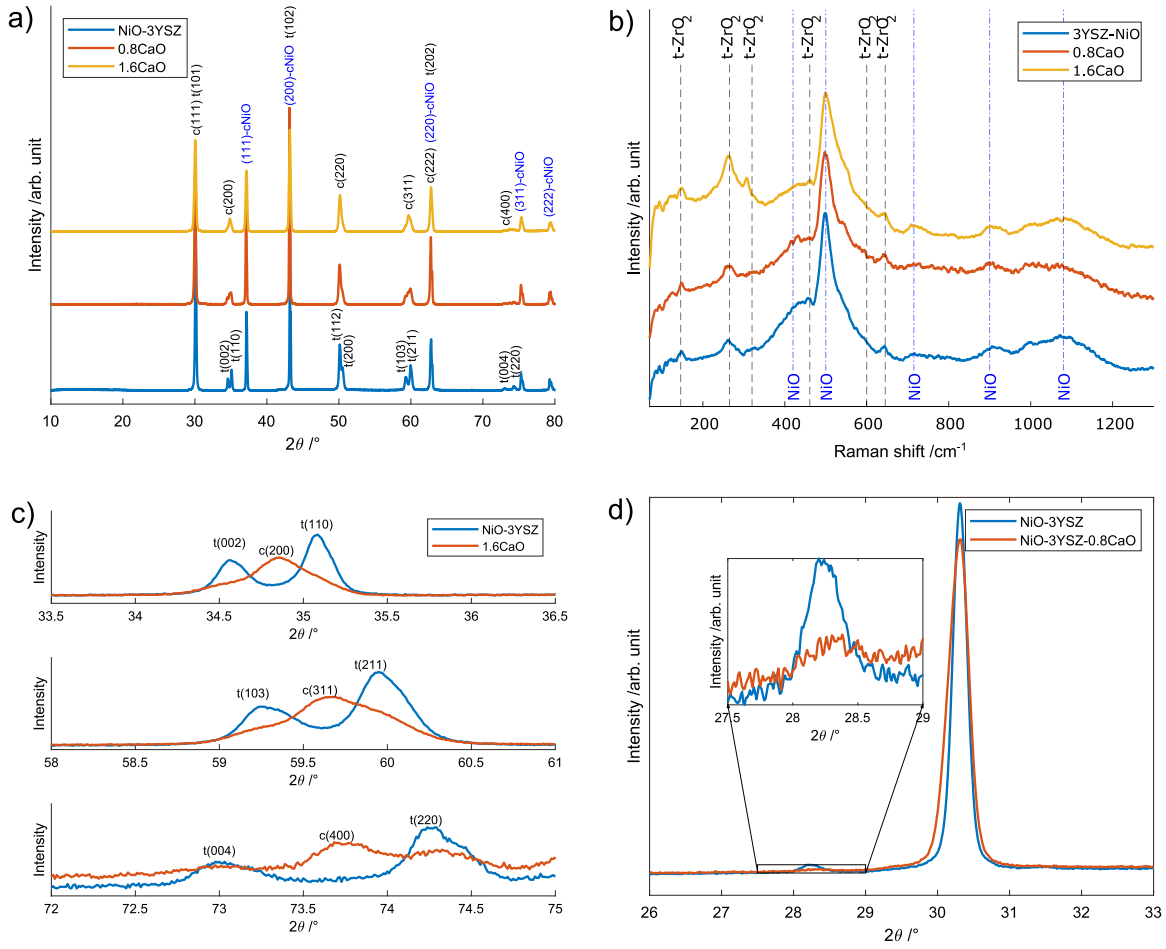

Fig. 9. XRD of NiO/3YSZ samples with different CaO contents shown in (a) with indexed peaks for tetragonal SZ (t), cubic SZ (c), and cubic NiO (c-NiO). In (b), the respective Raman spectra are illustrated with peaks marked for tetragonal ZrO_2 and NiO. Subfigure (c) shows a zoomed in view of the characteristic regions in which a cubic SZ peak emerges for the 1.6 mol% case compared to the pure NiO/3YSZ sample. In (d), the XRD of pure NiO/3YSZ and 0.8 mol% CaO co-doped NiO/3YSZ is depicted with the onset of the monoclinic peak (m-SZ) highlighted.

of hydrothermal degradation quantifiable by XRD. The trend is, as outlined for the grain size, contradictory to studies on Al_2O_3 [43], Nd_2O_3 [27], and La_2O_3 co-doped 3YSZ, which demonstrated a higher LTD rate with increasing dopant content [27].

A comparison between the properties of 2YSZ [43], 3YSZ [43], 4.3 mol% CaO stabilised ZrO_2 (4CSZ) [44], 0.4 mol% La_2O_3 co-doped 3YSZ [27], and 1.6 mol% CaO co-doped 2YSZ observed in this study can be seen in Table 3. All the samples were characterised to consist of the tetragonal phase but differ in the grain size, LTD kinetic rate b, hardness and toughness. While the hardness is similar between 2YSZ and 3YSZ, the fracture toughness was reported to be twice for 2YSZ. Interestingly, the toughness of 4CSZ was found to be nearly as high as for 2YSZ [43,44], which can be seen as promising indicator for a high toughness of the CaO co-doped 2YSZ prepared in this study that could be assessed in future works [44,45]. In terms of LTD rates, the co-doping of 2YSZ and 3YSZ or higher dopant concentration (3YSZ vs. 2YSZ) proofs beneficial, both measures reduce the rate compared with pure 2YSZ and 3YSZ. This shows for 2YSZ co-doped by CaO a correlation with the grain size. However, for 3YSZ the co-doping with La_2O_3 increases the grain size but lowers the LTD rate. This emphasises the different factors governing the LTD in stabilised zirconia and is discussed more below in the context of the findings of this study.

In the present study, the grain size reduces by 28% for 0.8 mol% CaO sintered with P3-1350-1250 °C and by 31% for P1-1250 °C, whereas the reduction is 35% and 38% for 1.6 mol% CaO, respectively. However, the minor reduction of grain size with 1.6 mol% CaO over 0.8 mol% cannot fully explain the strong suppression of LTD. For 1.6 mol% CaO co-doped 2YSZ, the suppression of LTD continues over the test duration of 50 h with 0.8 mol% CaO co-doped 2YSZ close to fully transforming into the monoclinic phase. This indicates an effect of CaO beyond the reduction of grain size on the mitigation of LTD.

The comparison between LTD rates and average grain sizes of P3-1350-1250 °C for plain 2YSZ and P1-1250 for 1.6 mol% CaO co-doped 2YSZ supports this observation. The former has an average grain size of 203 nm (P3-1350-1250 °C) and the latter one of 201 nm (P1-1250 °C). The densification is close between both samples with 98.6% for P3 and 99.0% for P2. If only the grain size would be the decisive factor in LTD of CaO co-doped 2YSZ, both should depict a comparable degradation rate. This is not the case and pure 2YSZ (P3-1350-1250 °C) reaches a monoclinic volume fraction of 100% after 20 h of testing, whereas 1.6 mol% CaO co-doped 2YSZ (P2-1450 °C) shows a monoclinic volume fraction of 2% at the same time.

Those observations highlight the significant effect of co-doping with CaO beyond the reduction of the average grain size. Some established findings on doping of SZ with CaO can offer explanations for the additional suppression of LTD:

1. **Oxygen vacancies**: The CaO co-doping introduces additional oxygen vacancies into 2YSZ, moving the concentration away from the critical threshold for the phase transformation to monoclinic, as was previously hypothesised [10,27]. The divalent Ca also forms one oxygen vacancy ($Ca''_{Zr} + V_O^{\bullet\bullet}$) per doped cation compared with the trivalent Y, which forms one vacancy for two cations ($2\,Y'_{Zr} + V_O^{\bullet\bullet}$).

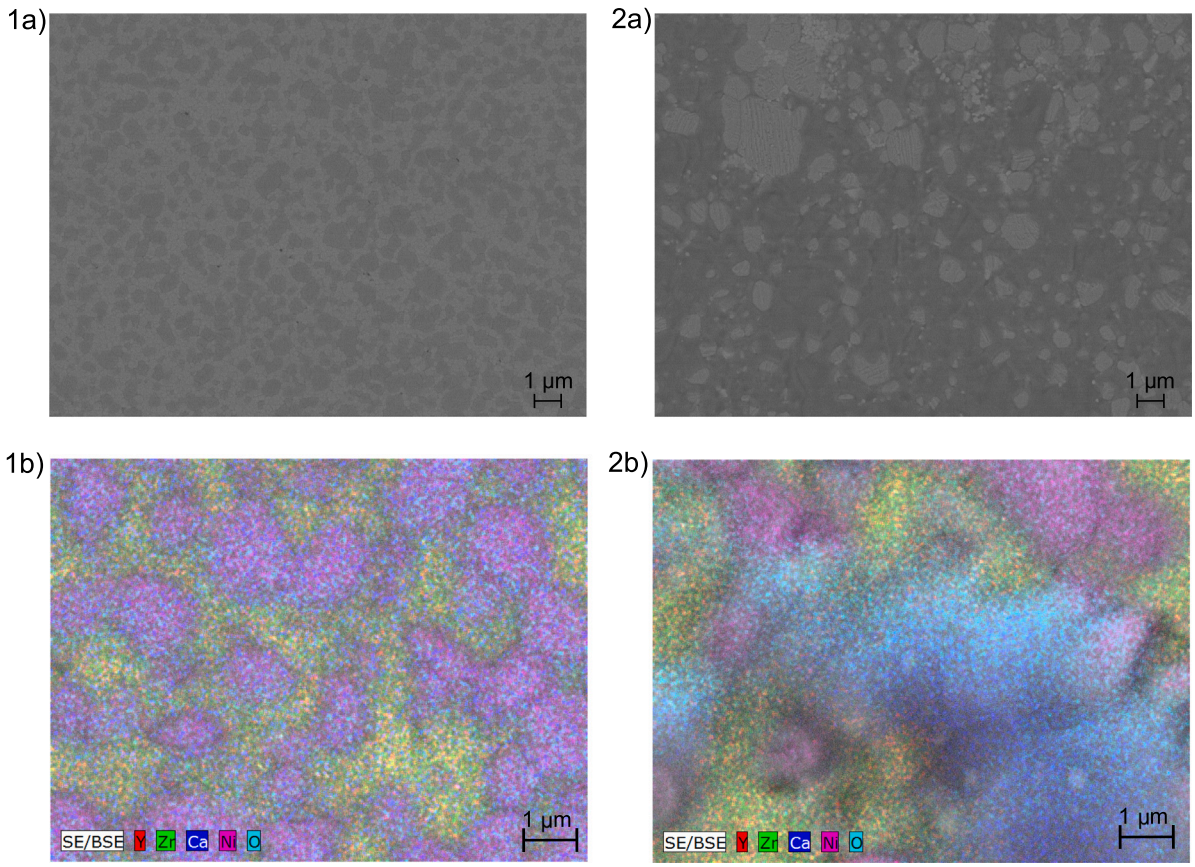

Fig. 10. Backscattered electron images of the NiO/3YSZ samples surface shown in (1a) and for 1.6 mol% CaO co-doped NiO/3YSZ in (2a) with the phase contrast between NiO, 3YSZ and secondary CaO phase visible. In (1b) and (2b), SEM-EDS maps of the NiO/3YSZ and 1.6 mol% CaO co-doped surface are shown highlighting the secondary CaO phase for the latter.

Table 3
Table comparing the grain size, LTD rate, hardness and toughness of various tetragonal stabilised zirconia systems.

	2YSZ [43]	3YSZ [43]	4.3 mol% CaO-SZ [44]	0.4 mol% La_2O_3-3YSZ [27]	1.6 mol% CaO-2YSZ
Grain size /nm	292	211	100	332	201
Sintering temperature /°C	1450 (2 h)	1450 (2 h)	1250 (2 h)	1500 (2 h)	1450 (3 min)
LTD rate b /h^{-1}	0.52	0.08	–	0.02	0.04
Hardness /kg mm^{-2}	1239	1304	–	–	–
Toughness / MPa $m^{1/2}$	8.6	4.1	8.3	–	–

2. **Bulk and grain boundary transport**: CaO in the host lattice of YSZ could limit the transport of oxygen species (hydroxyls and oxygen ions) from the surface exposed to H_2O into the bulk or along grain boundaries. The favoured segregation of Ca to grain boundaries and surface originates from the different valance charge and cationic radius of Ca^{2+} compared with Y^{3+} and Zr^{4+} [66,69–72]. The limited oxygen species transport with Ca-doping can also be observed in the lower ionic conductivity of Ca- compared with Y-stabilised zirconia [69,73]. In addition, space charge at grain boundaries and surface due to alkali earth segregation, as found for other fluorite doped ceramics (gadolinia doped ceria) [27,74], could further restrict grain boundary transport by CaO doping.
3. **Surface kinetics and oxygen exchange**: CaO segregation to the surface of 2YSZ could further alter the surface kinetics for insertion of O-species into the oxygen vacancies of 2YSZ due to modified electronic properties of the surface that changes with Ca in CaO doped zirconia [72]. Recent studies indicate the role of co-dopants, Nb^{5+} in the referenced case, on the oxygen exchange kinetics of YSZ [75]. In addition, trace amounts of Ca impurities were previously found to form a several monolayer thin and Ca rich phase at the surface of YSZ [67].

The short summary of related literature can explain the additional suppression of LTD by CaO co-doping through the defect concentration (oxygen vacancies) and segregation of CaO to surface and grain boundaries. Both affect the kinetics and uptake of H_2O related species and the transport in the bulk and over grain boundaries.

4.4. NiO/3YSZ composite and CaO co-doping

The findings for the CaO co-doping can be reproduced in the composite of NiO/3YSZ with a reduced grain size of 185 nm for 0.8 mol% CaO co-doping compared to 234 nm in the plain case. Moreover, the autoclave tests over 124 h indicate a suppression of LTD in the composite co-doped with 0.8 mol% CaO.

In contrast to the 2YSZ samples, we found secondary phase formation when adding 1.6 mol% CaO to NiO/3YSZ. The phase consists of CaO analysed by SEM-EDS, with a precise chemical composition analysis outside the scope of this study. As the amount of CaO was added according to the composite of NiO and 3YSZ, the precise fraction in relation to 3YSZ is 2.3 mol% for 0.8 mol% CaO co-doped NiO/3YSZ and 4.6 mol% for 1.6 mol% CaO co-doped NiO/3YSZ. The high dopant content in the 1.6 mol% CaO co-doped case leads to the formation of some cubic phase, as is shown in Fig. 9, which also agrees well with

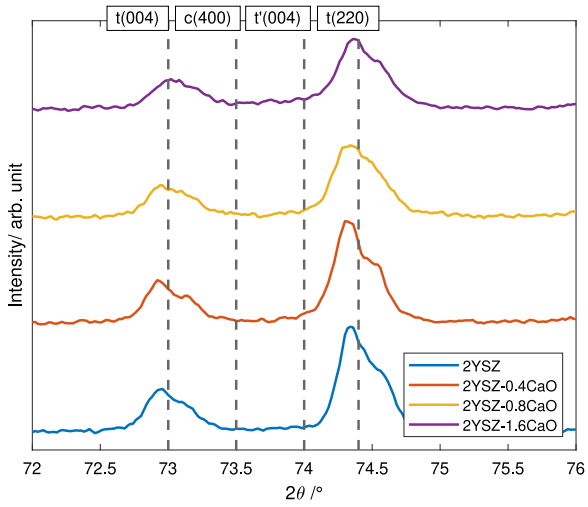

Fig. 11. Comparison of XRD in the 2θ range of 72–76° for P1-1250 °C and pure 2YSZ, 0.4, 0.8, and 1.6 mol% CaO co-doped 2YSZ.

reported cubic phase formation for CaO stabilised ZrO_2 in the respective CaO amount range relative to 3YSZ [44,45] Such high co-dopant contents were not tested with 2YSZ and indicate a limit in the solubility of CaO in 3YSZ. Since CaO segregates to the grain boundaries [66], the solubility limit would predominantly concern a narrow region around the grains. Once the limit is surpassed, the uptake of CaO will be constrained and a secondary CaO phase can form around the grains, as observed by SEM-EDS as well as can cause the transformation from tetragonal into the cubic phase as measured by XRD.

Interactions of Ca with YSZ were also previously reported and the authors observed $CaZrO_3$ and CaO formation [76,77]. A calcium zirconate phase was not detected here but it emphasises the mobility of Ca in the zirconia matrix. These previous observations and our results indicate the solubility limit of CaO in YSZ (here above 3 mol% CaO in 3YSZ). Further studies could investigate the applicability of this route for solid oxide cells operated at temperatures above 600 °C when additional mobility of Ca might occur and interactions with other materials could deteriorate performance.

Nonetheless, the findings outline a promising route to mitigate LTD in mechanical Ni/3YSZ support structures of SOCs, which are due to the porosity around 30% [48] more susceptible to the degradation in contrast to the dense NiO/3YSZ samples of this study.

5. Conclusion

In this study, we investigated two routes to mitigate LTD in 2YSZ and the composite of 3YSZ and nickel oxide. For the former, a reduction in grain size is achieved through the addition of 0.4, 0.8, and 1.6 mol% of CaO and two-step sintering. For the latter, the co-doping of 0.8 mol% of CaO decreased the grain size up to 20%. Both methods achieve the reduction in grain size of 2YSZ and 3YSZ/NiO without compromising densification.

The systematic investigation of eight different sintering programs for pure 2YSZ, 0.4, 0.8, and 1.6 mol% co-doped 2YSZ presents useful quantitative information in terms of assessing sintering of 2YSZ according to grain size and densification. Tracking the volume fraction of monoclinic phase with ageing further yields characteristic degradation parameter for 2YSZ and CaO co-doped 2YSZ. The extension of CaO doping to 3YSZ/NiO confirms that the effects are not unique to 2YSZ but also have relevance for the solid oxide cell technology.

The three main findings are: (1) the reduction in average grain size of 2YSZ and 3YSZ in the composite with NiO following the two-step sintering with comparable densification to conventional sintering, (2) the mitigation of LTD in 2YSZ and 3YSZ with the co-doping with calcium oxide, and (3) the additional suppression of LTD by Ca beyond the reduction in grain size of 2YSZ. The methods showcase the capabilities in limiting LTD of t-2YSZ and t-3YSZ. Hence, two-step sintering and co-doping with CaO can be valuable routes in producing tetragonal YSZ more resilient to hydrothermal degradation.

This study indicates that the effect of CaO co-doping on LTD of 2YSZ extends beyond the sole reduction in grain size. Future research could be directed towards a phenomenological understanding of CaO on the oxygen species uptake from humid environments and transport in the bulk and over grain boundaries. Furthermore, the findings of this study outline a possible route to LTD-resistant tetragonal zirconia with even lower yttria contents than in 2YSZ.

CRediT authorship contribution statement

Julian Taubmann: Writing – review & editing, Writing – original draft, Visualization, Methodology, Investigation, Formal analysis, Conceptualization. **Henrik Lund Frandsen:** Writing – review & editing, Project administration, Funding acquisition, Conceptualization. **Peyman Khajavi:** Writing – review & editing, Supervision, Methodology, Conceptualization.

Declaration of competing interest

The authors declare that they have no known competing financial interests or personal relationships that could have appeared to influence the work reported in this paper.

Acknowledgements

The authors gratefully acknowledge the funding by the Innovation Fund Denmark (IFD) under File No. 9067-00036B REFORGE.

References

[1] J. Chevalier, What future for zirconia as a biomaterial? Biomaterials 27 (4) (2006) 535–543.
[2] V. Lughi, V. Sergo, Low temperature degradation-aging-of zirconia: A critical review of the relevant aspects in dentistry, Dent. Mater. 26 (8) (2010) 807–820.
[3] J. Chevalier, L. Gremillard, S. Deville, Low-temperature degradation of zirconia and implications for biomedical implants, Annu. Rev. Mater. Res. 37 (2007) 1–32.
[4] J.L. Masonis, R.B. Bourne, M.D. Ries, R.W. McCalden, A. Salehi, D.C. Kelman, Zirconia femoral head fractures: a clinical and retrieval analysis, J. Arthroplasty 19 (7) (2004) 898–905.
[5] X.Q. Cao, R. Vassen, D. Stöver, Ceramic materials for thermal barrier coatings, J. Eur. Ceram. Soc. 24 (1) (2004) 1–10.
[6] L. Chen, Yttria-stabilized zirconia thermal barrier coatings—a review, Surf. Rev. Lett. 13 (05) (2006) 535–544.
[7] X.J. Chen, K.A. Khor, S.H. Chan, L.G. Yu, Influence of microstructure on the ionic conductivity of yttria-stabilized zirconia electrolyte, Mater. Sci. Eng. A 335 (1–2) (2002) 246–252.
[8] H. Uchida, M. Yoshida, M. Watanabe, Effect of ionic conductivity of zirconia electrolytes on the polarization behavior of various cathodes in solid fuel cells, J. Electrochem. Soc. 146 (1) (1999) 1.
[9] M.B. Mogensen, Materials for reversible solid oxide cells, Curr. Opin. Electrochem. 21 (2020) 265–273.
[10] J. Chevalier, L. Gremillard, A.V. Virkar, D.R. Clarke, The tetragonal-monoclinic transformation in zirconia: lessons learned and future trends, J. Am. Ceram. Soc. 92 (9) (2009) 1901–1920.
[11] H. Scott, Phase relationships in the zirconia-yttria system, J. Mater. Sci. 10 (1975) 1527–1535.
[12] H. Schmalzried, Chemical Kinetics of solids, VCH, Verlag, Weinheim, 1995.
[13] P. Li, I.-W. Chen, J.E. Penner-Hahn, Effect of dopants on zirconia stabilization—an X-ray absorption study: I, trivalent dopants, J. Am. Ceram. Soc. 77 (1) (1994) 118–128.
[14] P. Li, I.-W. Chen, J.E. Penner-Hahn, Effect of dopants on zirconia stabilization—an x-ray absorption study: II, tetravalent dopants, J. Am. Ceram. Soc. 77 (5) (1994) 1281–1288.

[15] P. Li, I.-W. Chen, J.E. Penner-Hahn, Effect of dopants on zirconia stabilization—an x-ray absorption study: III, charge-compensating dopants, J. Am. Ceram. Soc. 77 (5) (1994) 1289–1295.
[16] R.C. Garvie, R. Hannink, R. Pascoe, Ceramic steel? Nature 258 (5537) (1975) 703–704.
[17] R.H.J. Hannink, P.M. Kelly, B.C. Muddle, Transformation toughening in zirconia-containing ceramics, J. Am. Ceram. Soc. 83 (3) (2000) 461–487.
[18] K. Kobayashi, H. Kuwajima, T. Masaki, Phase change and mechanical properties of ZrO2-Y2O3 solid electrolyte after ageing, Solid State Ion. 3 (1981) 489–493.
[19] S. Ramesh, K.S. Lee, C. Tan, A review on the hydrothermal ageing behaviour of Y-TZP ceramics, Ceram. Int. 44 (17) (2018) 20620–20634.
[20] J. Chevalier, B. Cales, J.M. Drouin, Low-temperature aging of Y-TZP ceramics, J. Am. Ceram. Soc. 82 (8) (1999) 2150–2154.
[21] S. Fabris, A.T. Paxton, M.W. Finnis, A stabilization mechanism of zirconia based on oxygen vacancies only, Acta Mater. 50 (20) (2002) 5171–5178.
[22] G. Pezzotti, M.C. Munisso, A.A. Porporati, K. Lessnau, On the role of oxygen vacancies and lattice strain in the tetragonal to monoclinic transformation in alumina/zirconia composites and improved environmental stability, Biomaterials 31 (27) (2010) 6901–6908.
[23] X. Guo, Property degradation of tetragonal zirconia induced by low-temperature defect reaction with water molecules, Chem. Mater. 16 (21) (2004) 3988–3994.
[24] D.T. Chaopradith, D.O. Scanlon, C.R.A. Catlow, Adsorption of water on yttria-stabilized zirconia, J. Phys. Chem. C 119 (39) (2015) 22526–22533.
[25] X. Guo, Hydrothermal degradation mechanism of tetragonal zirconia, J. Mater. Sci. 36 (2001) 3737–3744.
[26] F. Zhang, K. Vanmeensel, M. Batuk, J. Hadermann, M. Inokoshi, B. Van Meerbeek, I. Naert, J. Vleugels, Highly-translucent, strong and aging-resistant 3Y-TZP ceramics for dental restoration by grain boundary segregation, Acta Biomater. 16 (2015) 215–222.
[27] F. Zhang, M. Batuk, J. Hadermann, G. Manfredi, A. Mariën, K. Vanmeensel, M. Inokoshi, B. Van Meerbeek, I. Naert, J. Vleugels, Effect of cation dopant radius on the hydrothermal stability of tetragonal zirconia: grain boundary segregation and oxygen vacancy annihilation, Acta Mater. 106 (2016) 48–58.
[28] A. Samodurova, A. Kocjan, M.V. Swain, T. Kosmač, The combined effect of alumina and silica co-doping on the ageing resistance of 3Y-TZP bioceramics, Acta Biomater. 11 (2015) 477–487.
[29] I. Ross, W. Rainforth, D. McComb, A. Scott, R. Brydson, The role of trace additions of alumina to yttria–tetragonal zirconia polycrystals (Y–TZP), Scr. Mater. 45 (6) (2001) 653–660.
[30] K. Shah, J. Holloway, I. Denry, Effect of coloring with various metal oxides on the microstructure, color, and flexural strength of 3Y-TZP, J. Biomed. Mater. Res. Part B Appl. Biomater. J. Soc. Biomater. Jpn. Soc. Biomater. Aust. Soc. Biomater. Korean Soc. Biomater. 87 (2) (2008) 329–337.
[31] K. Syed, M. Xu, K.K. Ohtaki, D. Kok, K.K. Karandikar, O.A. Graeve, W.J. Bowman, M.L. Mecartney, Correlations of grain boundary segregation to sintering techniques in a three-phase ceramic, Materialia 14 (2020) 100890.
[32] H.B. Lee, F.B. Prinz, W. Cai, Atomistic simulations of grain boundary segregation in nanocrystalline yttria-stabilized zirconia and gadolinia-doped ceria solid oxide electrolytes, Acta Mater. 61 (10) (2013) 3872–3887.
[33] H. Li, S. Dey, R.H. Castro, Kinetics and thermodynamics of densification and grain growth: Insights from lanthanum doped zirconia, Acta Mater. 150 (2018) 394–402.
[34] M. Inokoshi, F. Zhang, J. De Munck, S. Minakuchi, I. Naert, J. Vleugels, B. Van Meerbeek, K. Vanmeensel, Influence of sintering conditions on low-temperature degradation of dental zirconia, Dent. Mater. 30 (6) (2014) 669–678.
[35] F. Zhang, K. Vanmeensel, M. Inokoshi, M. Batuk, J. Hadermann, B. Van Meerbeek, I. Naert, J. Vleugels, 3Y-TZP ceramics with improved hydrothermal degradation resistance and fracture toughness, J. Eur. Ceram. Soc. 34 (10) (2014) 2453–2463.
[36] R. Riedel, I.-W. Chen, Ceramics Science and Technology, John Wiley & Sons, 2012.
[37] R.A. Terpstra, P. Pex, A.H. de Vries, Ceramic processing, Springer, 1995.
[38] S.A. Basha, D. Sarkar, Grain growth suppression of ZTA by multi-step sintering, Mater. Today. Proc. 26 (2020) 1226–1230.
[39] I.-W. Chen, X.-H. Wang, Sintering dense nanocrystalline ceramics without final-stage grain growth, Nature 404 (6774) (2000) 168–171.
[40] M. Mazaheri, A. Simchi, F. Golestani-Fard, Densification and grain growth of nanocrystalline 3Y-TZP during two-step sintering, J. Eur. Ceram. Soc. 28 (15) (2008) 2933–2939.
[41] A. Bravo-Leon, Y. Morikawa, M. Kawahara, M.J. Mayo, Fracture toughness of nanocrystalline tetragonal zirconia with low yttria content, Acta Mater. 50 (18) (2002) 4555–4562.
[42] W. Xue, Z. Xie, J. Yi, J. Chen, Critical grain size and fracture toughness of 2 mol.% yttria-stabilized zirconia at ambient and cryogenic temperatures, Scr. Mater. 67 (12) (2012) 963–966.
[43] F. Zhang, K. Vanmeensel, M. Inokoshi, M. Batuk, J. Hadermann, B. Van Meerbeek, I. Naert, J. Vleugels, Critical influence of alumina content on the low temperature degradation of 2–3 mol% yttria-stabilized TZP for dental restorations, J. Eur. Ceram. Soc. 35 (2) (2015) 741–750.
[44] W. Pyda, K. Haberko, CaO-containing tetragonal ZrO2 polycrystals (Ca-TZP), Ceram. Int. 13 (2) (1987) 113–118.
[45] R. Pampuch, W. Pyda, K. Haberko, The obtainment and properties of calcia-TZP, Ceram. Int. 14 (4) (1988) 245–249.
[46] P. Khajavi, P.V. Hendriksen, J. Chevalier, L. Gremillard, H.L. Frandsen, Improving the fracture toughness of stabilized zirconia-based solid oxide cells fuel electrode supports: Effects of type and concentration of stabilizer (s), J. Eur. Ceram. Soc. 40 (15) (2020) 5670–5682.
[47] P. Khajavi, H.L. Frandsen, L. Gremillard, J. Chevalier, P.V. Hendriksen, Strength and hydrothermal stability of NiO–stabilized zirconia solid oxide cells fuel electrode supports, J. Eur. Ceram. Soc. 41 (7) (2021) 4206–4216.
[48] D.-W. Ni, B. Charlas, K. Kwok, T.T. Molla, P.V. Hendriksen, H.L. Frandsen, Influence of temperature and atmosphere on the strength and elastic modulus of solid oxide fuel cell anode supports, J. Power Sources 311 (2016) 1–12.
[49] I.O. Owate, R. Freer, Thermochemical etching method for ceramics, J. Am. Ceram. Soc. 75 (5) (1992) 1266–1268.
[50] R.C. Garvie, P.S. Nicholson, Phase analysis in zirconia systems, J. Am. Ceram. Soc. 55 (6) (1972) 303–305.
[51] H. Toraya, M. Yoshimura, S. Somiya, Calibration curve for quantitative analysis of the monoclinic-tetragonal ZrO2 system by X-ray diffraction, J. Am. Ceram. Soc. 67 (6) (1984) C–119.
[52] P. Halstead, A. Moore, The thermal dissociation of calcium hydroxide, J. Chem. Soc. (1957) 3873–3875.
[53] D. Beruto, L. Barco, A.W. Searcy, G. Spinolo, Characterization of the porous CaO particles formed by decomposition of CaCO3 and Ca(OH)2 in vacuum, J. Am. Ceram. Soc. 63 (7–8) (1980) 439–443.
[54] V. Bouineau, M. Pijolat, M. Soustelle, Characterisation of the chemical reactivity of a CaCO3 powder for its decomposition, J. Eur. Ceram. Soc. 18 (9) (1998) 1319–1324.
[55] A. Hills, The mechanism of the thermal decomposition of calcium carbonate, Chem. Eng. Sci. 23 (4) (1968) 297–320.
[56] Y. Wang, W.J. Thomson, The effect of sample preparation on the thermal decomposition of CaCO3, Thermochim. Acta 255 (1995) 383–390.
[57] J.-F. Li, R. Watanabe, Phase transformation in Y2O3-partially-stabilized ZrO2 polycrystals of various grain sizes during low-temperature aging in water, J. Am. Ceram. Soc. 81 (10) (1998) 2687–2691.
[58] A. Feinberg, C. Perry, Structural disorder and phase transitions in ZrO2-Y2O3 system, J. Phys. Chem. Solids 42 (6) (1981) 513–518.
[59] D.-J. Kim, H.-J. Jung, I.-S. Yang, Raman spectroscopy of tetragonal zirconia solid solutions, J. Am. Ceram. Soc. 76 (8) (1993) 2106–2108.
[60] D. Gazzoli, G. Mattei, M. Valigi, Raman and X-ray investigations of the incorporation of Ca2+ and Cd2+ in the ZrO2 structure, J. Raman Spect. Int. J. Aspects Raman Spectr. Incl. High. Order Process. Brillouin Rayleigh Scattering 38 (7) (2007) 824–831.
[61] F. Lange, Transformation toughening: Part 3 experimental observations in the ZrO2-Y2O3 system, J. Mater. Sci. 17 (1982) 240–246.
[62] P. Khajavi, Y. Xu, H.L. Frandsen, J. Chevalier, L. Gremillard, R. Kiebach, P.V. Hendriksen, Tetragonal phase stability maps of ceria-yttria co-doped zirconia: From powders to sintered ceramics, Ceram. Int. 46 (7) (2020) 9396–9405.
[63] L. Gremillard, J. Chevalier, T. Epicier, S. Deville, G. Fantozzi, Modeling the aging kinetics of zirconia ceramics, J. Eur. Ceram. Soc. 24 (13) (2004) 3483–3489.
[64] N. Mironova-Ulmane, A. Kuzmin, I. Steins, J. Grabis, I. Sildos, M. Pärs, Raman scattering in nanosized nickel oxide NiO, J. Phys. Conf. Ser. 93 (1) (2007) 012039.
[65] P. Salunkhe, M.A. AV, D. Kekuda, Investigation on tailoring physical properties of nickel oxide thin films grown by dc magnetron sputtering, Materials Research Express 7 (1) (2020) 016427.
[66] M. Aoki, Y.-M. Chiang, I. Kosacki, L.J.-R. Lee, H. Tuller, Y. Liu, Solute segregation and grain-boundary impedance in high-purity stabilized zirconia, J. Am. Ceram. Soc. 79 (5) (1996) 1169–1180.
[67] J. Nowotny, M. Sloma, W. Weppner, Surface relaxation of Y2O3-stabilized ZrO2, Solid State Ion. 28 (1988) 1445–1450.
[68] K. Matsui, H. Yoshida, Y. Ikuhara, Grain-boundary structure and microstructure development mechanism in 2–8 mol% yttria-stabilized zirconia polycrystals, Acta Mater. 56 (6) (2008) 1315–1325.
[69] J. Gong, Y. Li, Z. Tang, Z. Zhang, Enhancement of the ionic conductivity of mixed calcia/yttria stabilized zirconia, Mater. Lett. 46 (2–3) (2000) 115–119.
[70] A. Nakamura, J.B. Wagner, Defect structure, ionic conductivity, and diffusion in calcia-stabilized zirconia, J. Electrochem. Soc. 127 (11) (1980) 2325.
[71] W. Zhu, S. Nakashima, E. Marin, H. Gu, G. Pezzotti, Annealing-induced off-stoichiometric and structural alterations in Ca2+-and Y3+-stabilized zirconia ceramics, Materials 14 (19) (2021) 5555.

[72] J. Ramírez-González, A.R. West, Electrical properties of calcia-stabilised zirconia ceramics, J. Eur. Ceram. Soc. 40 (15) (2020) 5602–5611.
[73] L. Momenzadeh, I.V. Belova, G.E. Murch, A study of the thermal, ionic conductivities and thermotransport of calcia and gadolinia doped zirconia using molecular dynamics simulations, Solid State Ion. 387 (2022) 116061.
[74] X. Xu, Y. Liu, J. Wang, D. Isheim, V.P. Dravid, C. Phatak, S.M. Haile, Variability and origins of grain boundary electric potential detected by electron holography and atom-probe tomography, Nature Mater. 19 (8) (2020) 887–893.
[75] T. Bak, E.D. Wachsman, K.E. Prince, K.A. Rahman, J. Nowotny, In situ surface monitoring of charge transfer during oxidation of zirconia at elevated temperatures, ACS Appl. Energy Mater. 2 (4) (2019) 2810–2817.
[76] J. Carter, C. Appel, M. Mogensen, Reactions at the calcium doped lanthanum chromite–yttria stabilized zirconia interface, J. Solid State Chem. 122 (2) (1996) 407–415.
[77] K. Sasaki, T. Hayashi, M. Asakura, M. Ando, T. Kawai, S. Ban, Improving biocompatibility of zirconia surface by incorporating Ca ions, Dent. Mater. J. 34 (3) (2015) 336–344.